Regular Article

Synergistic use of smart materials for vibration-based energy harvesting

L.L. Silva[1], S.A. Oliveira[1], P.M.C.L. Pacheco[1], and M.A. Savi[2]

[1] CEFET/RJ, Department of Mechanical Engineering, 20.271.110 Rio de Janeiro, RJ, Brazil

[2] Universidade Federal do Rio de Janeiro, COPPE, Department of Mechanical Engineering, Center for Nonlinear Mechanics, 21.941.972 Rio de Janeiro, RJ, Brazil

Abstract. Vibration-based energy harvesting is an approach where available mechanical vibration energy is converted into electrical energy that can be employed for different purposes. This paper deals with the synergistic use of smart materials for energy harvesting purposes. In essence, piezoelectric and shape memory alloys are combined to build an energy harvesting system. The combined effect of these materials can increase the system performance and reduce some limitations. The possibility to control the mechanical stiffness under vibration by a shape memory alloy (SMA) element can provide the ability to tune resonant frequencies in order to increase the output power. The analysis is developed considering a one-degree of freedom mechanical system where the restitution force is provided by an SMA element. The electro-mechanical coupling is provided by a piezoelectric element. Linear piezoelectric constitutive equation is employed together with the Brinson's model for SMA element. Numerical simulations are carried out showing different responses of the system indicating that the inclusion of the SMA element can be used to extend the operational range of the system.

1 Introduction

Vibration-based energy harvesting is a promising area where environmental available mechanical vibration energy is converted into electrical energy that can be employed for different purposes. This idea has an increasing importance due to the necessity to generate energy, even if this is related to small amounts. Electronic device charging is a major application of the harvested energy, being related to either day-by-day life or sensors and actuators. Different kinds of potential applications are investing in this kind of idea using distinct mechanical systems as bridges, buildings, airplanes, cars and buoy structure [9,18,22,25].

Piezoelectric materials are usually employed for electro-mechanical conversion due to high output power density and energy conversion efficiency [1,7,10,11]. The great nowadays challenge is to increase the energy harvester performance, increasing the generated power for a specific vibration level.

In this regard, nonlinear effects have been incorporated to the systems. Mechanical, electrical and electro-mechanical coupling can be exploited. Besides, nonlinear descriptions can reduce inconsistencies predicted by linear models [21,24]. Nonlinear systems have been developed to obtain better performances over a broad frequency range providing more power than linear systems. The emblematic example of mechanical nonlinearities is the use of Duffing type oscillators with monostable [14,20] and bistable harvesters. The addition of two opposing permanent magnets to a piezoelectric cantilever beam is a possible way to introduce nonlinearities on the mechanical systems [6,8,9,23]. Betts et al. [4] presented a nonlinear device through an arrangement of bistable composites combined with piezoelectric elements for broadband energy harvesting of ambient vibrations. Results showed that is possible to improve the power harvested over conventional devices. Bai et al. [3] showed that an asymmetry tip mass can induce nonlinear and hysteretic behavior in the piezoelectric energy harvester with a free-standing thick-film bimorph structure.

Constitutive nonlinearities of the piezoelectric coupling are also important for a proper description of energy harvesting system. Triplett and Quinn [24] compared the influence of linear and nonlinear piezoelectric elements. Silva et al. [21] investigated the influence of hysteretic behavior of piezoelectric elements, showing the possibility to explore this kind of dissipation to obtain an optimum performance.

Random effect influences are another aspect that needs to be considered in energy harvesting devices. Usually, resonant-based energy harvesting is employed trying to obtain the best system performance. Because of that, any deviation from the resonance frequency can significantly reduce the output power. Therefore, random effects introduce difficulties for the tuned excitation frequency establishment. De Paula et al. [6] discussed the random effects on piezoelectric energy harvesting systems.

Another challenge that can be exploited in energy harvesting systems is the synergistic use of smart materials. Shape Memory Alloys (SMAs) can be combined with piezoelectric material in order to improve system performance through the control of system response. SMAs can be used to include adaptive dissipation associated with hysteretic behavior and mechanical property changes due to phase transformation. The property changes can alter dynamical characteristics of the system, allowing the adaptive tuning related to varying excitations [19]. Rhimi and Lajnef [17] studied the power, frequency and time response of a cantilevered composite beam containing piezoelectric ceramic and shape memory alloy cylindrical inclusions, showing the nonlinear behavior due to the phase transformation within the SMA inclusions. Avirovik et al. [2] developed a hybrid device coupling piezoelectric element with SMA for dual functionality, both as an actuator and an energy harvester.

This paper deals with the synergistic use of smart materials for energy harvesting purposes. In essence, piezoelectric and shape memory alloys are combined to build an energy harvesting system. A one-degree of freedom mechanical system is coupled to an electrical circuit by a piezoelectric element and the restitution force is provided by an SMA element. Linear piezoelectric constitutive equation is employed together with the Brinson's model for SMA thermomechanical description [5]. Numerical simulations are carried out showing different responses of the system. Results indicate that the vibration of the energy harvesting system can be tuned within a broadband frequency by using the SMA element at different temperatures.
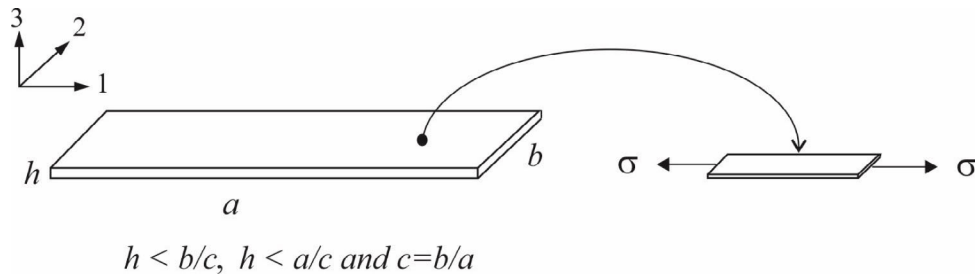
$h < b/c,\ h < a/c\ and\ c=b/a$

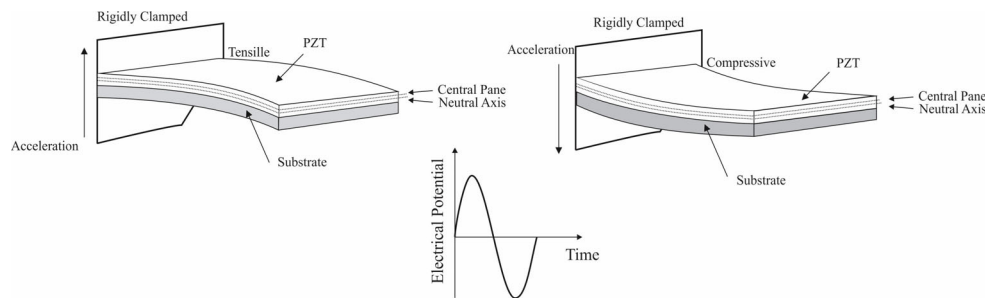**Fig. 1.** Thin piezoelectric beam.

Fig. 2. Schematic picture of a piezoelastic energy harvesting beam system.

2 Piezoeelectric constitutive model

Piezoelectric materials present electromechanical coupling being possible as direct and inverse modes. The inverse effect is associated with the generation of strain/stress in response to an applied electrical field; on the other hand, the direct effect is related to electrical charge that is a response to an applied strain/stress. If the piezoelastic behavior of a thin structure is such that it can be modeled as a beam, the stress components other than the one-dimensional bending normal stress are negligible, see Fig. 1, where c represents the width-length ratio, which typically should be 1:2 [12]. The 1-D constitutive equations are given by [10]:

$$\varepsilon = s^{\psi_E}\sigma + \varrho\psi_E \quad \text{(inverse effect)} \tag{1}$$

$$D = \varrho\sigma + \kappa^{\sigma}\psi_E \quad \text{(direct effect)} \tag{2}$$

where ε is the strain, σ is the stress, D is the electric displacement, and ψ_E is the electric field. The elastic compliance, piezoelectric coupling and permittivity are denoted respectively by s, ϱ and κ. The superscripts ψ_E and σ denote that the respective constants are evaluated at constant electric field and stress, respectively.

A usual configuration of an energy harvesting system is based on a cantilever beam, shown in Fig. 2. Basically, the piezoelectric beam generator has one piezoelectric layer attached to a substrate rigidly clamped at one end. The PZT beam operating in a bending mode is subjected either to tensile or compressive stresses and produces electrical voltage, Fig. 2 [12].
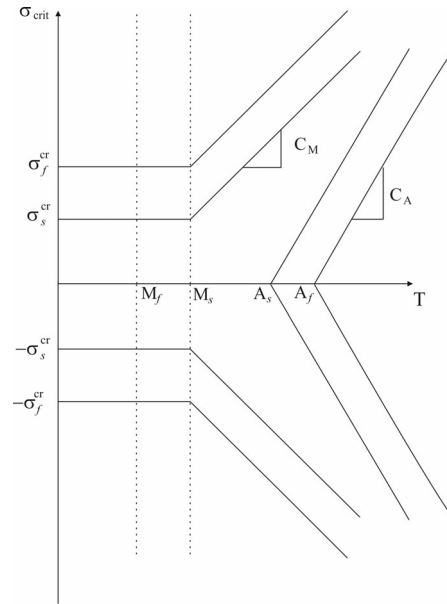
Fig. 3. Phase transformation diagram representing critical stresses for phase transformation and martensitic reorientation.

3 Shape memory alloy constitutive model

Shape memory alloys (SMAs) present thermo-mechanical coupling and its description can be done by different ways [13,15]. Here, the one-dimensional constitutive model originally proposed by [5] is modified to incorporate tension-compression behavior.

The description of the SMA behavior considers an internal variable that represent martensitic volume fraction, ξ. The evolution of this variable is based on the kinetics of the phase transformation that establishes a function of temperature, T, and one-dimensional strain, ε. In Brinson's model, two distinct parts compose the martensitic volume fraction: temperature induced martensitic, ξ_T, and stress induced martensitic, ξ_S. Therefore, $\xi = \xi_T + \xi_S$.

The proposed model extends the model for tension-compression description establishing that the martensitic volume fraction, ξ, is decomposed into a temperature induced part, ξ_T, a tension stress induced part, ξ_+, and a compression stress induced part, ξ_-, resulting in $\xi = \xi_T + \xi_+ + \xi_-$. The thermo-mechanical behavior of the SMA is described by the following equation:

$$\dot{\sigma} = E\dot{\varepsilon} + \Omega\dot{\xi}_+ - \Omega\dot{\xi}_- + \Theta\dot{T} \tag{3}$$

where σ is the stress and E is the Young modulus that can be defined as a function of ξ as $E = E_A + \xi\left(E_M - E_A\right)$, where E_A and E_M are the austenite and martensite Young modulus, respectively. The parameter Ω is associated with phase transformation being defined as $\Omega = -E\varepsilon_L$, where ε_L is the maximum residual strain. The parameter Θ is related to thermal expansion, being defined as $\Theta = -E\alpha$, where α is the thermal expansion coefficient.

The phase transformation kinetics is defined by prescribed functions. Basically, it is considered phase transformation critical points, defined from the phase transformation diagram, presented in Fig. 3. In this regard, it is possible to define the following parameters: M_s and M_f- start and finish temperatures of martensite transformation, respectively; A_s and A_f – start and finish temperatures of austenite transformation,

respectively; σ_s^{cr} and σ_f^{cr} – critical stress for martensite transformation start and finish, respectively. C_A and C_M are material properties related to the relations between transformation stresses and temperature showed in the Fig. 3.

Based on transformation diagram, it is possible to define regions where macroscopic phase transformations take place and also the evolution equations. Note that volume fractions need to obey the restriction: $0 \leq \xi \leq 1$. The conversion from austenite or twinned martensite to detwinned martensite is described as follows:

- For $T > M_s, \sigma_s^{cr} + C_M (T - M_s) < |\sigma| < \sigma_f^{cr} + C_M (T - M_s)$

$$\xi_S = \frac{1 - \xi_S^0}{2} \cos \left\{ \frac{\pi}{\sigma_s^{cr} - \sigma_f^{cr}} \left[\sigma - \sigma_f^{cr} - C_M (T - M_s) \right] \right\} + \frac{1 + \xi_S^0}{2} \tag{4}$$

$$\xi_T = \xi_T^0 - \frac{\xi_T^0}{1 - \xi_S^0} \left(\xi_S - \xi_S^0 \right) \tag{5}$$

where $\xi_S = \xi_+$ if $\sigma > 0$, and $\xi_S = \xi_-$ if $\sigma < 0$. Moreover, the superscript 0 that appears in ξ_S^0 and ξ_T^0, represent the volume fraction at the beginning of the phase transformation.

- For $T < M_s$ and $\sigma_s^{cr} < |\sigma| < \sigma_f^{cr}$

$$\xi_S = \frac{1 - \xi_S^0}{2} \cos \left\{ \frac{\pi}{\sigma_s^{cr} - \sigma_f^{cr}} \left[\sigma - \sigma_f^{cr} \right] \right\} + \frac{1 + \xi_S^0}{2} \tag{6}$$

$$\xi_T = \xi_T^0 - \frac{\xi_T^0}{1 - \xi_S^0} \left(\xi_S^0 - \xi_S^0 \right) + \Delta_T \xi \tag{7}$$

where $\xi_S = \xi_+$ if $\sigma > 0$, and $\xi_S = \xi_-$ if $\sigma < 0$.

When $M_f < T < M_s$ and $T < T_0$

$$\Delta_T \xi = \frac{1 - \xi_T^0}{2} \left\{ \cos \left[a_M (T - M_f) \right] + 1 \right\} \tag{8}$$

$$\Delta_T \xi = 0 \text{ , otherwise.}$$

The kinetic functions for reverse transformations, from martensite to austenite is given by:

- For $T > A_s$ and $C_A (T - A_f) < |\sigma| < C_A (T - A_s)$

$$\xi = \frac{\xi^0}{2} \left\{ \cos \left[a_A \left(T - A_s - \frac{\sigma}{C_A} \right) \right] + 1 \right\} \tag{9}$$

$$\xi_S = \xi_S^0 - \frac{\xi_S^0}{\xi^0} \left(\xi^0 - \xi \right) \tag{10}$$

$$\xi_T = \xi_T^0 - \frac{\xi_T^0}{\xi^0} \left(\xi^0 - \xi \right) \tag{11}$$

where $\xi_S = \xi_+$ if $\sigma > 0$, and $\xi_S = \xi_- if \sigma < 0$.

Constants a_M and a_A are defined by the following expressions:

$$a_M = \frac{\pi}{M_s - M_f} \text{ and } a_A = \frac{\pi}{A_f - A_s}. \tag{12}$$
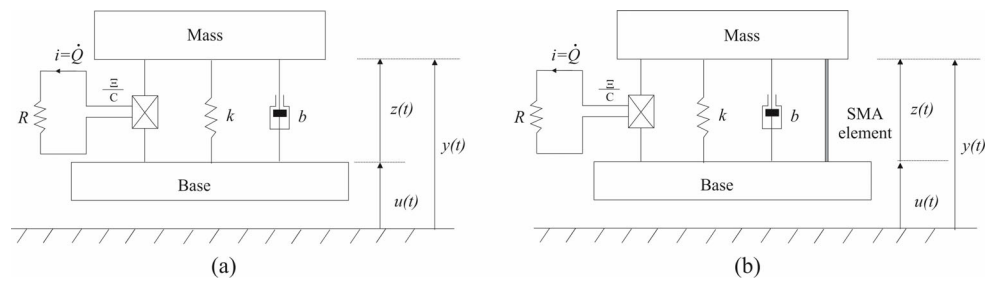
Fig. 4. Archetypal models of the vibration-based energy harvesting system: mechanical oscillator connected to an electrical circuit by a piezoelectric element. (a) Classical system. (b) Piezoelectric-SMA system exploiting the synergistic use of smart materials.
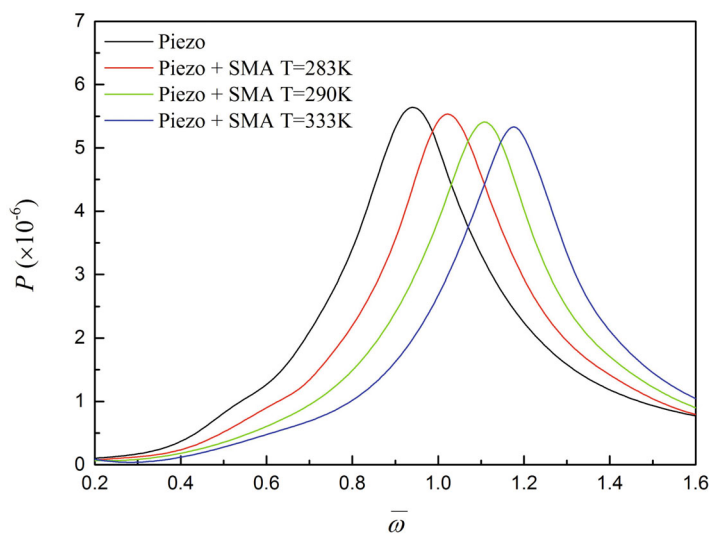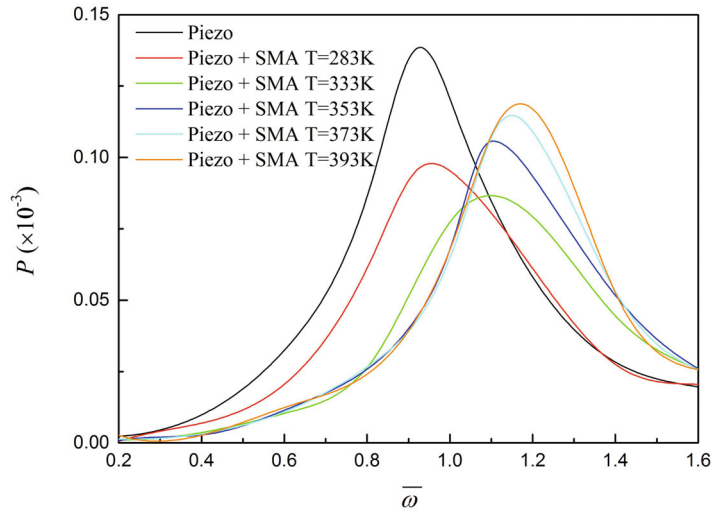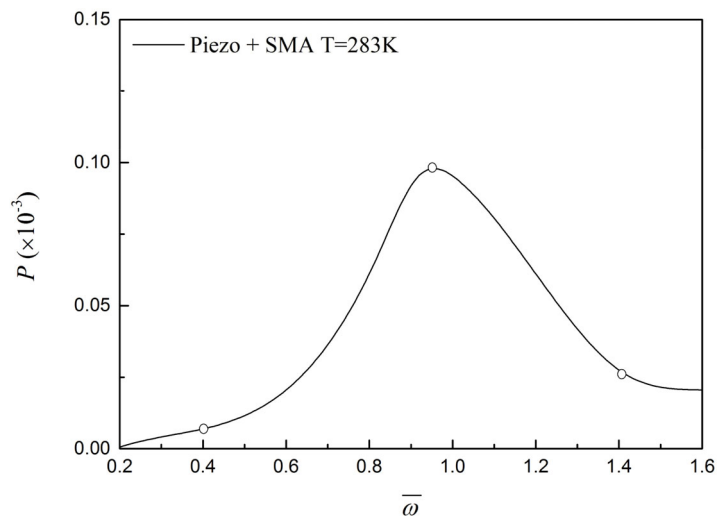

Fig. 5. Maximum non-dimensional power versus frequency: comparison between classical and a system incorporating an SMA element at different temperatures ($\delta = 0.001$).

4 Vibration-based energy harvesting

An archetypal model for the vibration-based energy harvesting system is build by considering a mechanical system connected to an electrical circuit by a piezoelectric element, responsible for the electro-mechanical conversion. A mass-spring-damper oscillator with mass, m, stiffness k, and a linear viscous coefficient b, represents the mechanical system. This system is subjected to a base excitation $u = u(t)$, and the mass displacement is represented by y; z is the mass displacement relative to the base. An electrical resistance, R, represents the electrical circuit and Q denotes the electrical charge. The electro-mechanical coupling is provided by the piezoelectric element being represented by Ξ. The synergistic use of smart materials is performed by incorporating an SMA element to this archetypal model. Figure 4 presents both situations and, in essence, the SMA element may be considered as a bar with length l and cross-sectional area A, presenting a restitution force F_R.

Table 1. Shape memory alloy parameters.

E_A (GPa)	E_M (GPa)	ε_L	Θ (MPa/K)
69	23	0.055	0.55
σ_s(MPa)	σ_f(GPa)	C_A(MPa/K)	C_M(MPa/K)
90	170	8.5	9
M_f(K)	M_s(K)	A_s(K)	A_f(K)
285	295	320	333

Fig. 6. Maximum non-dimensional power versus frequency: comparison between classical and a system incorporating an SMA element at different temperatures ($\delta = 0.005$).

Fig. 7. Maximum non-dimensional power versus frequency for a system incorporating an SMA element at 283 K ($\delta = 0.005$).
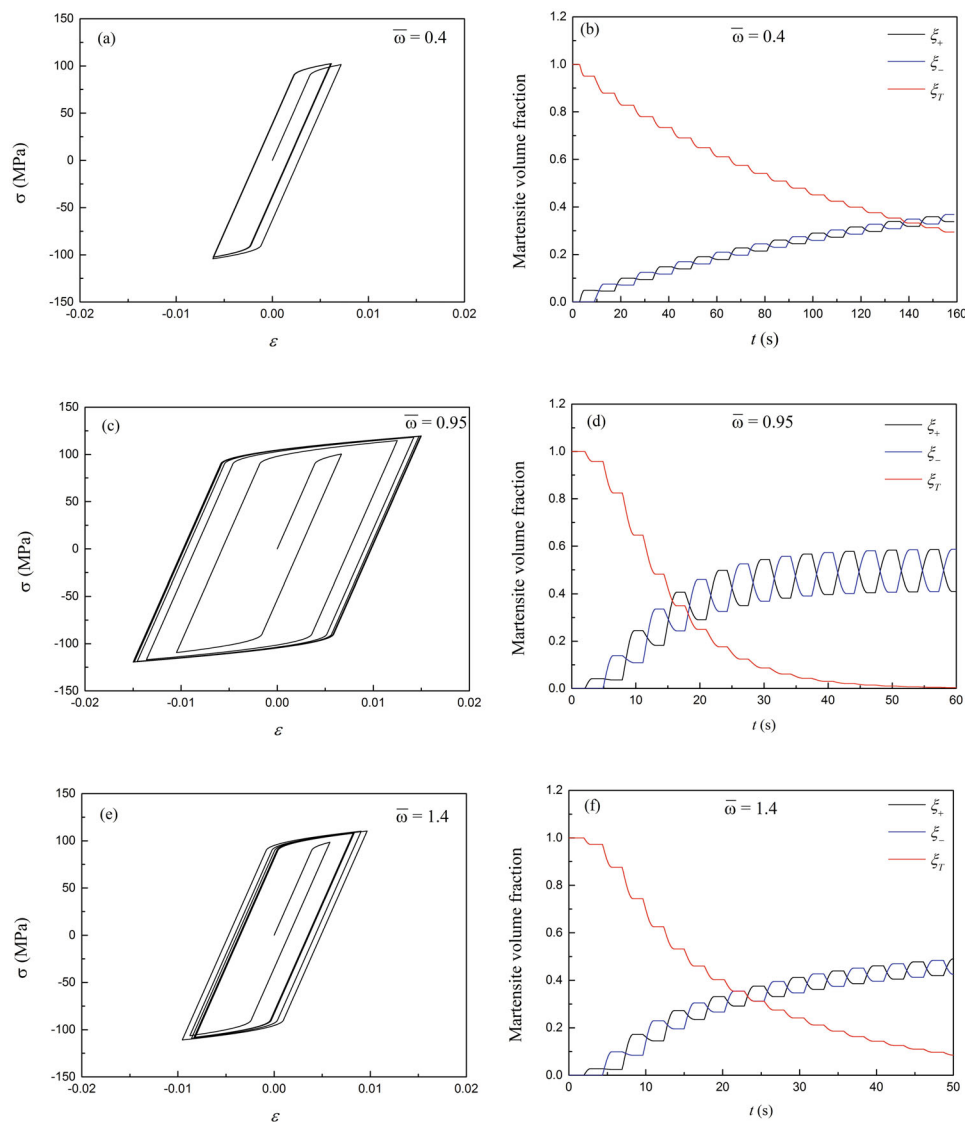
Fig. 8. Stress-strain curves and martensite volume fraction evolution for different frequencies of the points highlighted in Fig. 7 ($T = 283$ K).

The energy harvesting system dynamics (showed in Fig. 4) are described by the following equations of motion:

$$m\ddot{z} + bz + kz - \frac{\Xi}{C}Q + F_R = -m\ddot{u} \qquad (13)$$

$$R\dot{Q} - \frac{\Xi}{C}z + \frac{Q}{C} = 0 \qquad (14)$$

where $(\dot{\blacksquare}) \equiv d(\blacksquare)/dt$ and amplitude harmonic base acceleration is $-\ddot{u} = B\sin(\omega t)$. The classical system dynamics (Fig. 4(a)) can be obtained adopting $F_R = 0$. On the other hand, the system dynamics incorporating the SMA element (Fig. 4(b)) is described with the restitution force, $F_R = \sigma A$, where σ is described by the constitutive
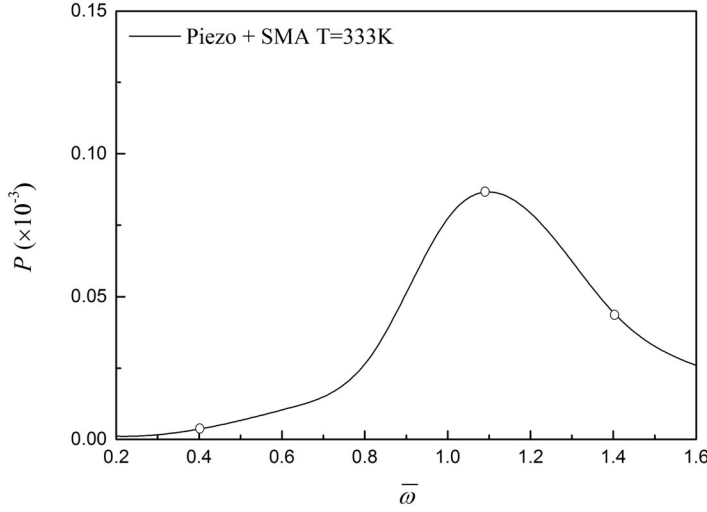
Fig. 9. Maximum non-dimensional power versus frequency for a system incorporating an SMA element at $333\,\mathrm{K}$ ($\delta = 0.005$).

equations presented in the previous section, see Eq. (3). Therefore, the mechanical part of the equation of motion can be written as:

$$m\ddot{z} + b\dot{z} + kz + A[E\varepsilon + \Omega(\xi_+ - \xi_-) + \Theta T + g_0] - \frac{\Theta}{C}Q = -m\ddot{u} \qquad (15)$$

where $g_0 = \sigma_0 - E\varepsilon_0 - \Omega\left(\xi_+^0 - \xi_-^0\right) - \Theta T_0$. In order to obtain a non-dimensional system, new coordinates $x = z/l$, $U = u/l$ and $x = \varepsilon$ are defined. Moreover, it is assumed $Q = Q_0 q$, and $\tau = \omega_0 t$, where Q_0 is a constant with dimension of charge and $\omega_0 = \sqrt{k/m}$ is a frequency. Using, $\varsigma = b/m\omega_0$, $\mu_{\mathrm{E}} = EA/m\omega_0^2 l$, $\epsilon = Q_0^2/m\omega_0^2 Cl^2$, $\Phi = (l/Q_0)\,\Xi$, $\rho = RC\omega_0$, $\bar{\Omega} = \Omega A/m\omega_0^2 l$, $\bar{\theta} = \theta A/m\omega_0^2 l$, $\bar{g}_0 = g_0 A/m\omega_0^2 l$, $\bar{\omega} = \omega/\omega_0$ and $\delta = -B/\omega_0^2 l$, the equations for vibration-based energy harvesting system can be rewritten as follows (Fig. 4a):

$$x'' + \varsigma x' + x - \epsilon\Phi q = \delta\sin\left(\bar{\omega}\tau\right) \qquad (16)$$

$$\rho q' + q - \Phi x = 0 \qquad (17)$$

where $(\blacksquare)' \equiv d(\blacksquare)/d\tau$, with τ being the non-dimensional time [24]. When the SMA element is incorporated to the system (Fig. 3(b)), the equations can be rewritten as follows:

$$x'' + \varsigma x' + x + \mu_E x + \bar{\Omega}(\xi_+ - \xi_-) + \bar{\theta}T + \bar{g}_0 + \epsilon\Phi q = \delta\sin(\bar{\omega}\tau) \qquad (18)$$

$$\rho q' + q - \Phi x = 0. \qquad (19)$$

The instantaneous non-dimensional electrical power is evaluated using the equation $P = \rho(q')^2$. Numerical simulations are performed by employing the operator split technique together with an iterative process. Basically, the state space is split into dynamical and constitutive variables. Dynamical variables include position, velocity and electrical variables. The fourth order Runge-Kutta method is employed to integrate this space assuming that the constitutive variables, essentially associated with
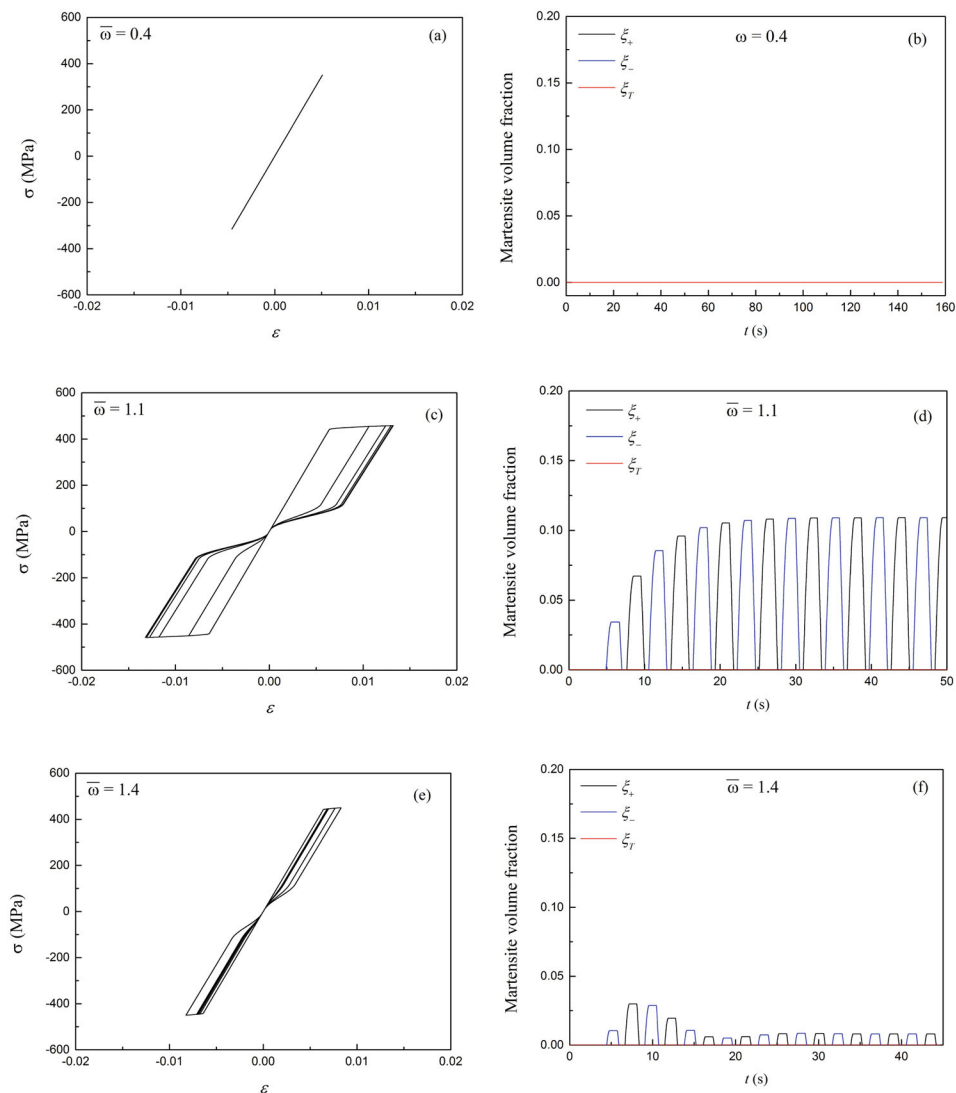
Fig. 10. Stress-strain curves and martensite volume fraction evolution for different frequencies of the points highlighted in Fig. 9 ($T = 333$ K).

volume fractions, are known. This result is used as an input for the constitutive space. A predictor-corrector procedure is then applied using strain-driving case. For a specific strain, a trial stress is calculated. If the trial state is not feasible, a projection is carried out. The constitutive integration evaluates new constitutive variables that are employed to recalculate the dynamical space. This procedure continues until a prescribed tolerance is reached. The following parameters are adopted for all simulations: $\varsigma = 0.2$, $\rho = 1.0$, $\epsilon = 0.2$ and $\Phi = 1.0$. Concerning SMA properties, Table 1 presents typical values for SMAs that are employed for simulations [5].

5 Numerical simulations

This section discusses numerical simulations of the energy harvesting system establishing a comparison between classical model and the system incorporating an SMA
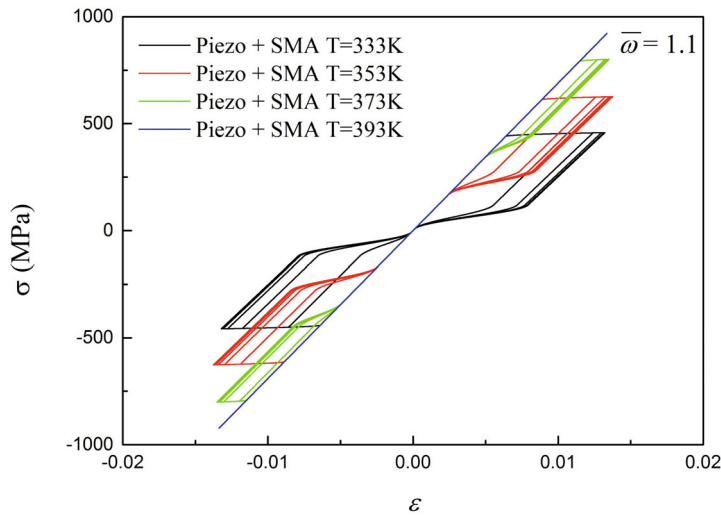
Fig. 11. Stress-strain curves for different temperatures ($\bar{\omega} = 1.1$).
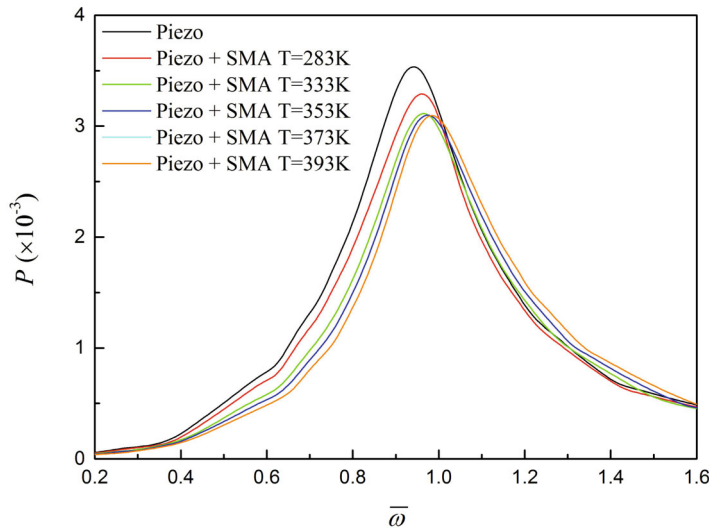

Fig. 12. Maximum non-dimensional power versus frequency: comparison between classical and a system incorporating an SMA element at different temperatures ($\delta = 0.025$).

element. Different temperatures are analyzed exploring the shape memory and pseudoelastic effects. The analysis starts by considering small base excitation amplitudes of motion that does not induce stress-induced phase transformation, presenting only elastic response. This is done by assuming a base excitation amplitude of $\delta = 0.001$.

Figure 5 shows results of maximum non-dimensional power versus frequency. The system with SMA element is treated for different temperatures: $T = 283\,\text{K}$, a low temperature where martensite is stable for a stress-free state; $T = 290\,\text{K}$, an intermediate temperature where martensite and austenite may coexist for a stress-free state; and $T = 333\,\text{K}$, representing a high temperature where austenitic phase is stable for a stress-free state. Note that the increase of the temperature of the SMA element tends to attenuate the amplitude response in comparison with the classical model, and in
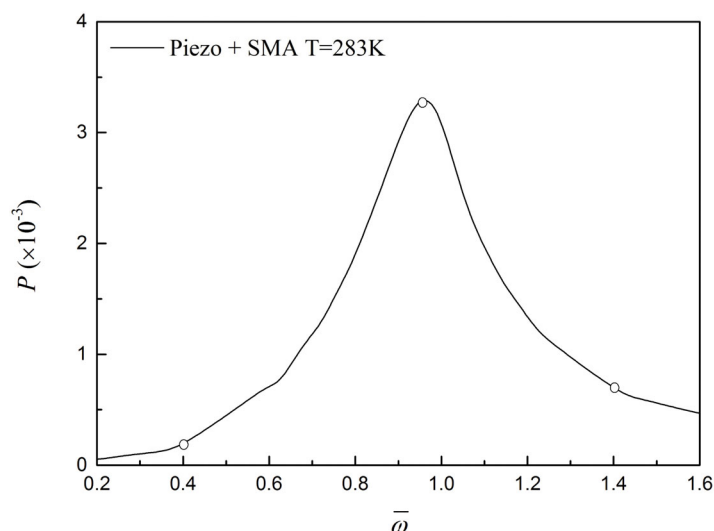
Fig. 13. Maximum non-dimensional power versus frequency for a system incorporating an SMA element at 283 K ($\delta =0.025$).

addition, tends to shift maximum value of the power curve to the right. This is due to the SMA element stiffness variation associated with the change of Young modulus, dependent of the volume fraction ξ, promoted by temperature variation. Under the small base excitation amplitudes, the SMA element experiments an elastic response, and the stiffness depends only on its temperature. Therefore, temperature variations that are not associated with phase transformations, below M_f (285 K) and above A_f (333 K), do not change power-frequency curves. It should be highlighted that the inclusion of the SMA element can improve the system performance. By increasing the temperature from 283 K to 333 K, the system can operate from a base excitation frequency associated with the low temperature peak amplitude ($\bar{\omega} = 1.1$) to the one related to the high temperature peak amplitude ($\bar{\omega} = 1.2$) with only a small amplitude reduction of less than 5%. The system without the SMA element presents an amplitude reduction larger than 50% for a variation of the base excitation frequency of the same order (10%).

Higher base excitation amplitudes are now in focus by considering $\delta = 0.005$. Under this condition, stress-induced phase transformation occurs and therefore, two effects affect the dynamical behavior of the system: SMA element stiffness variation promoted by the dependence of the Young modulus on the volume fraction phase; and the dissipation associated with the hysteretic behavior. Figure 6 shows that the increase of temperature for austenitic phase tends to promote the increase of the peak power and still shifting it to the right in comparison with the previous case where the peak remains at the same value for any temperature above A_f. These results show that temperature variations can change the peak frequencies and also reduce the undesired system amplitude reduction, being an essential advantage in terms of energy harvesting.

A better comprehension of this effect is provided through the stress-strain curves and the phase transformation evolution, represented by the martensitic volume fraction evolution. Initially, low temperature behavior is of concern. Figure 7 shows the power amplitudes where three points at different frequencies are highlighted. The corresponding stress-strain curves for these three points are presented in Fig. 8 showing hysteretic behavior associated with incomplete phase transformation. At $\bar{\omega} = 0.95$,
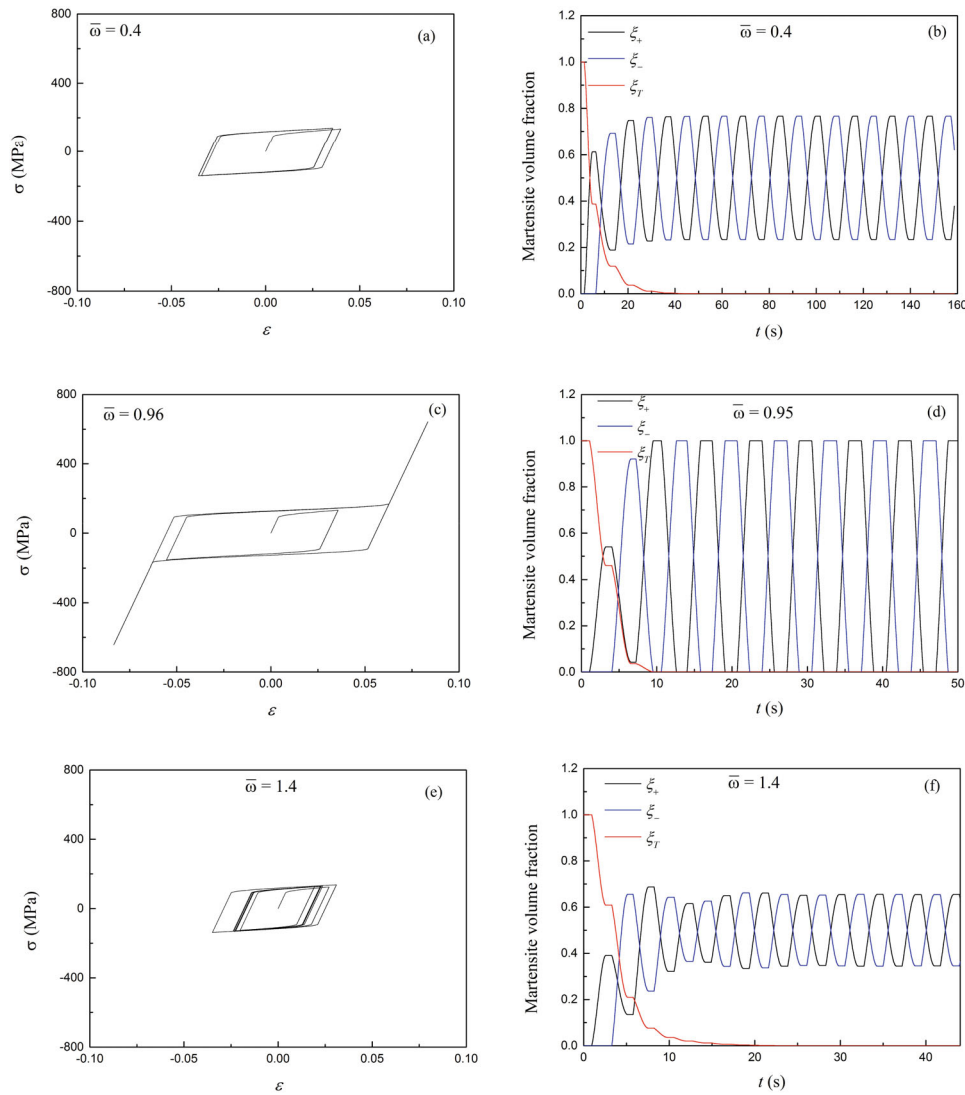
Fig. 14. Stress-strain curves and martensite volume fraction evolution for different frequencies for the points highlighted in Fig. 13 ($T = 283\,\mathrm{K}$).

there is a significant increase of hysteresis loop caused by larger strain values (resonant frequency). By continuing to increase the frequency, the hysteresis loop starts to become smaller. Based on that, it is possible to observe that stiffness variation and hysteretic behavior establish a competition that define the system response.

A higher temperature is now in focus ($T = 333\,\mathrm{K}$). The power curve is shown in Fig. 9 and Fig. 10 presents responses for the specific highlighted points. Note the linear behavior for $\bar{\omega} = 0.4$ where phase transformations do not occur. Once again, resonant response has larger amplitudes and therefore, more phase transformations occur being associated with higher dissipation due to hysteretic behavior ($\bar{\omega} = 1.1$). When $\bar{\omega} = 1.4$ the system presents phase transformation but with smaller amplitudes.

SMA element thermo-mechanical behavior is now analyzed by considering $\bar{\omega} = 1.1$ (resonant frequency) and different temperatures. Figure 11 presents stress-strain
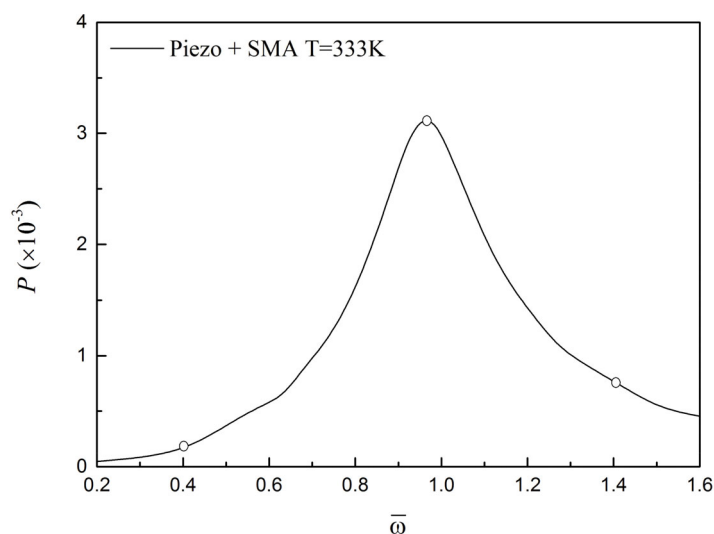
Fig. 15. Maximum non-dimensional power versus frequency for a system incorporating an SMA element at $333\,K$ ($\delta = 0.025$).

curves for different temperatures. This behavior explains the power peak increase and shift on frequency response with higher temperatures. Note that, the increase of temperature causes the increase of the critical stress level where phase transformation begins to occur. Therefore, the temperature increase is related to the higher position of the hysteresis loop in the stress-strain space, and as the strain values is limited for the same region, the hysteresis loop size decreases with the increase of temperature. At $T = 393\,K$ phase transformations do not take place anymore, and therefore, the response has a linear response, without hysteresis. These results correspond to a decrease in system dissipation modifying the generated power.

By increasing even more the base excitation motion amplitudes ($\delta = 0.025$) the system presents responses that tend to be closer for high and low temperature. The power peak values are quite similar and the shift on frequency almost disappears. Figure 12 shows the power curve for different temperatures. Low temperature power curve is presented in Fig. 13 and the corresponding stress-strain curves and martensitic volume fraction evolution for specific values are shown in Fig. 14. Note that complete phase transformations are observed when $\bar{\omega} = 0.96$.

High temperature system behavior is presented in Fig. 15 as a power curve. Figure 16 shows the corresponding stress-strain curves and martensitic volume fraction evolution for specific responses. The same behavior of the previous case is found and, at $\bar{\omega} = 0.96$, major hysteresis loop is reached being associated with complete phase transformations. Dissipation process due to hysteretic behavior tends to cause an approximation between the power curves at high and low temperatures. It should be pointed out that the temperature variations have a small influence to system performance for large amplitude behavior. But, of course, this is the best situation for energy harvesting and, therefore, it is not necessary to alter this situation.

Figure 17 shows stress-strain curves for $\bar{\omega} = 0.96$ at different temperatures. It is noticeable that dissipation due to hysteresis is quite similar for all temperatures and the behavior is almost the same for all cases. This is a different behavior compared with those related to small amplitudes.
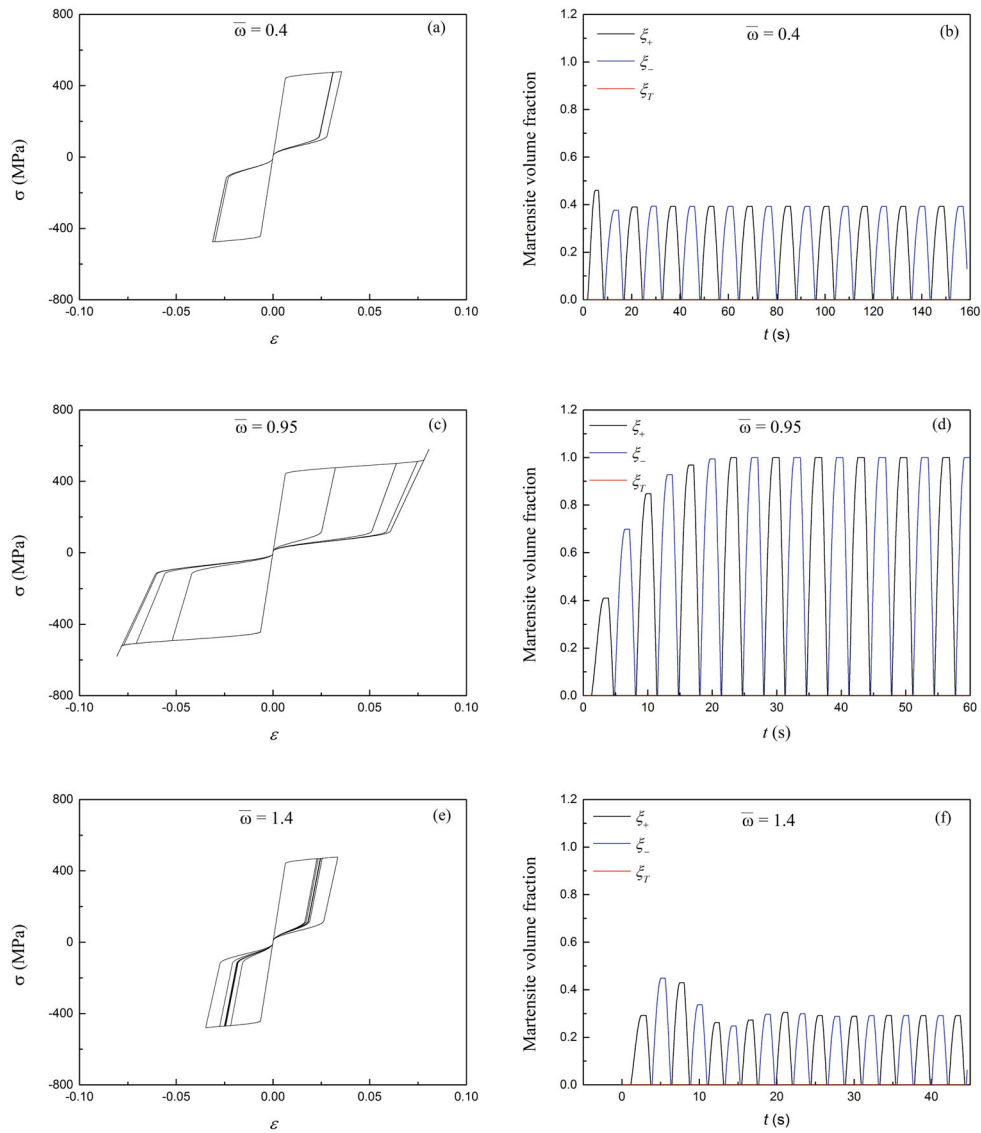
Fig. 16. Stress-strain curves and martensite volume fraction evolution for different frequencies for the points highlighted in Fig. 15 (temperature of 333 K).

6 Conlusions

The synergistic use of smart materials is discussed for energy harvesting purposes. In essence, piezoelectric and shape memory alloys are combined to build an energy harvesting system. A one-degree of freedom mechanical system, where the restitution force is provided by a combination of elastic and an SMA element, is coupled to an electrical circuit by a piezoelectric element. The main idea is to use temperature variations to enhance energy harvesting. Numerical simulations are carried out at different temperatures and motion amplitudes showing distinct responses of the system. Basically, it is possible to change the generated power amplitude and also to
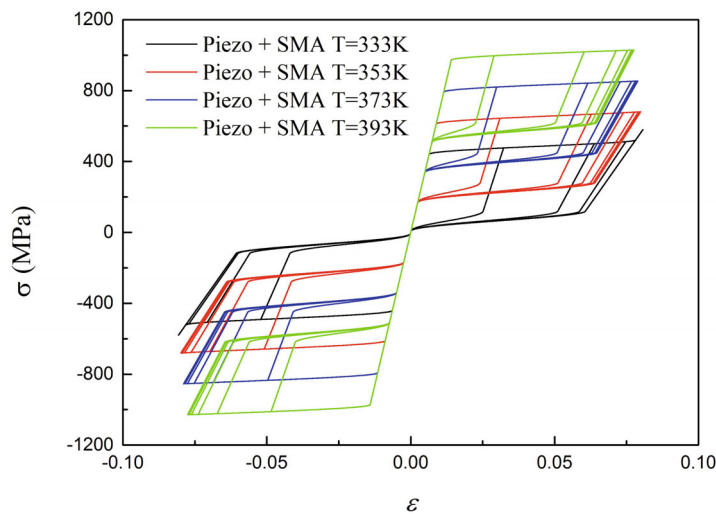
Fig. 17. Stress-strain curves for $\bar{\omega} = 0.96$ at different temperatures.

shift the peak of the power curve as a function of frequency. The piezoelectric-SMA system is temperature dependent and two major mechanisms should be highlighted to define system dynamics: stiffness change and dissipation due to hysteresis. For low amplitudes, the energy harvesting system can be tuned within a broadband frequency by using the SMA element at different temperatures. Under these conditions, stiffness change is the preponderant phenomenon. When high amplitudes are involved, stiffness change and hysteretic behavior establish a competition in order to define the system response. The increase of response amplitudes tends to approximate behaviors of the classical system and the one incorporating an SMA element at different temperatures. Both power and the shift on frequency are quite similar. Under these conditions, the harvested energy is as big as possible for classical system and therefore, there is no need to enhance system performance. In general, it is possible to say that the incorporation of the SMA element can be used to extend the operational range of the system, adjusting the system performance in terms of energy harvesting.

References

1. S.R. Anton, H.A. Sodano, Smart mater. Struct. **16**, 1 (2007)
2. D. Avirovik, A. Kumar, R.J Bodnar, S. Priya, Smart Mater. Struct. **22**, 052001 (2013)
3. Y. Bai, M. Carl, T.W. Button, Int. J. Struct. Stability Dyn. **14**, 1440016 (2014)
4. D.N. Betts, H.A. Kim, C.R. Bowen, D.J. Inman, Appl. Phys. Lett. **100**, 114104 (2012)
5. L.C. Brinson, J. Intel. Mater. Syst. Struct. **4**, 229 (1993)
6. A.S. De Paula, D.J. Inman, M.A. Savi, Mech. Syst. Signal Proc. **54**, 405 (2015)
7. N.E. Dutoit, B.L. Wardle, Integrated Ferroelectrics **83**, 13 (2006)
8. A. Erturk, J. Hoffmann, D.J. Inman, Appl. Phys. Lett. **94**, 254102 (2009)
9. A. Erturk, W.G.R. Vieira, De Marqui Jr. D.J. Inman, Appl. Phys. Lett. **96**, 184103 (2010)

10. A. Erturk, D.J. Inman (John Wiley & Sons, 2011a)
11. A. Erturk, D.J. Inman, J. Sound Vibration **330**, 2339 (2011b)
12. S.L. Kok, N.M. White, N.R. Harris, Measurement Science Techno. **20**, 124010 (2009)
13. D. Lagoudas, Shape Memory Alloys: Modeling and Engineering Applications (Springer, 2008)
14. B.P. Mann, N.D. Sims, J. Sound Vibration **319**, 515 (2009)
15. A. Paiva, M.A. Savi, Math. Problems Eng. **2006**, 1 (2006)
16. A. Ralib, A. Md, A.N. Nordin, H. Salleh, Microsystem Technol. **16**, 1673 (2010)
17. M. Rhimi, N. Lajnef, ASME 2012 Conference on Smart Mater. Adaptive Struct. Intel. Systems **2**, 19 (2012)
18. S. Roundy, D. Steingart, L. Frechette, P. Wright, J. Rabaey, Wireless Sensor Networks **2920**, 1 (2004)
19. M.A. Savi, Intel. J. Non-linear Mech. **70**, 2 (2015)
20. G. Sebald, H. Kuwano, D. Guyomar, B. Ducharne, Smart Mater. Struct. **20**, 102001 (2011)
21. L.L. Silva, P.C. Monteiro, M.A. Savi, T.A. Netto, J. Intel. Mater. Systems Struct. **24**, 1278 (2013)
22. H.A. Sodano, J.D. Inman, G. Park, Shock Vibration Digest **36**, 197 (2004)
23. S.C. Stanton, A. Erturk, B.P. Mann, D.J. Inman, J. Appl. Phys **108**, 074903 (2010)
24. A. Triplett, D.D. Quinn, J. Intel. Mater. Systems Struct. **20**, 1959 (2009)
25. N. Wu, Q. Wang, X. Xie, Appl. Ocean Res. **50**, 110 (2015)